High areal capacity cation and anionic redox solid-state batteries enabled by transition metal sulfide conversion

Grace Whang^{a,*}, Lukas Ketter^{a,b}, Tong Zhao^{a,b}, Elina Nazmutdinova^{a,b}, Marvin A. Kraft^c, Wolfgang G. Zeier ^{a,c,*}

^aInstitute of Inorganic and Analytical Chemistry, University of Münster, 48149 Münster, Germany

^bInternational Graduate School of Battery Chemistry, Characterization, Analysis, Recycling

and Application (BACCARA), University of Münster, 48149 Münster, Germany

^cForschungszentrum Jülich GmbH, Institute of Energy and Climate Research

Helmholtz-Institute Münster (IEK-12), 52425 Jülich, Germany

*Corresponding author email: whang @uni-muenster.de, wzeier @uni-muenster.de

Keywords: All solid-state batteries, conversion cathodes, transition metal sulfide, Li₂S, FeS **Abstract**

Pure sulfur (S₈ and Li₂S) all solid-state batteries inherently suffer from low electronic conductivities requiring the use of carbon additives, resulting in decreased active material loading at the expense of increased loading of the passive components. In this work, a transition metal sulfide in combination with lithium disulfide is employed as a dual cation-anion redox conversion composite cathode system. The transition metal sulfide undergoes cation redox, enhancing the electronic conductivity, whereas lithium disulfide undergoes anion redox, enabling high voltage redox conductive to achieving high energy densities. Carbon-free cathode composites with active material loadings above 6.0 mg cm⁻² attaining areal capacities of ~4 mAh cm⁻² are demonstrated with the possibility to further increase the active mass loading above 10 mg cm⁻² achieving cathode areal capacities above 6 mAh cm⁻², albeit with less cycle stability. In addition, the effective partial transport and thermal properties of the composites are investigated to better understand FeS:Li₂S cathode properties at the composite level. The work introduced here, provides an

alternative route and blueprint towards designing new dual conversion cathode systems which can operate without carbon additives enabling higher active material loadings and areal capacities.

Introduction

Rechargeable batteries play a critical role in the net zero carbon emissions by 2050 picture.¹ Rapidly growing demands in both the transportation and stationary energy storage sector for lithium-ion batteries require a careful balance between diversifying battery chemistries, assessing their environmental impact, and providing good electrochemical performance. The re-emergence of all solid-state batteries (SSB) with the discovery of fast room temperature solid-state electrolytes opens up an alternative path towards high energy density systems with the possibility of enhanced safety and circumvention of some challenges faced in liquid electrolyte batteries (flammability of the electrolyte solvent, polysulfide shuttling for Li-S systems, freezing of liquid electrolyte at low temperatures). For instance, while the current focus to look at commercialized cathodes, LiNi_{0.8}Co_{0.1}Mn_{0.1}O₂ and LiFePO₄ serves as the initial steps in bridging the gap between liquid and all solid-state batteries, ultimately, the benefits of moving to all solid-state systems are maximized when moving towards multi-electron redox conversion cathodes which can provide even greater capacities and thus energy densities. While LiNi_{0.8}Co_{0.1}Mn_{0.1}O₂ SSB provide good capacities with respect to intercalation chemistries, challenges in regard to interfacial stability remain and gaseous decomposition products pose safety concerns.^{2,3} On the other hand, LiFePO₄ SSB have recently gained traction as promising alternatives for both the electric vehicle and home storage applications. However, the low ionic and electronic conductivity of LiFePO₄ requires carbon additives resulting in lower energy densities at the cell level and there have been mixed reports on the stability and cyclability of LiFePO₄ SSB.⁴⁻⁶ Beyond LiNi_{0.8}Co_{0.1}Mn_{0.1}O₂ and LiFePO₄, there has been active research in exploring conversion chemistries such as elemental sulfur which undergo multi-electron redox processes providing a multi-fold increase in cathode capacity relative to their intercalation counterpart.⁷⁻⁹ Furthermore, moving to an all-solid-state system eliminates the long-standing issue of polysulfide shuttling faced in liquid electrolyte Li-S systems. However, the electronic and ionic insulating properties of the products formed during cycling (S₈ and Li₂S) require the use of carbon additives to establish triple phase boundaries between the active material, solid electrolyte, and conductive additive.⁸ Although carbon additives help to establish the electronic pathways within the cathode composite, they also increase the weight and volume of the passive components, reducing energy density at the cell level and have been shown to aggravate the decomposition of sulfide solid electrolytes.¹⁰ To address these challenges, strategies such as coatings and redox mediators have been explored.^{7,11-13} While progress on Li-S SSB continue, in parallel, it is imperative to explore other conversion chemistries that can also benefit from the lessons learned in the Li-S SSB community. Considering the challenges with poor electronic conductivity and sulfide solid electrolyte degradation aggravated by carbon, designing alternative systems that circumvent these issues is critical towards pushing the field forward and provide a broader perspective and alternative routes toward achieving high energy density all solid-state batteries.

Conversion transition metal sulfides are promising and re-emerging candidates as high energy density SSB cathodes (Fe-S, Cu-S, etc).^{14–17} While initially explored decades prior, ^{18,19} advancements in solid electrolytes, better understanding of ion and electron transport in cathode composites, and a growing need to diversify cathode chemistries, provide a new context to revisit these systems. In addition, many transition metal sulfides exhibit much higher electronic conductivities relative to their pure sulfur counterparts (S₈ and Li₂S) and produce electrochemically induced metallic frameworks from the reduction of the transition metal upon lithiation.^{20–22} The higher initial electronic conductivity prior to cycling in combination with the establishment of an electronic framework during cycling opens up the possibility to reduce or eliminate the use of carbon completely. FeS₂ is one of the most popular transition metal sulfide conversion cathodes due its high earth abundance, non-toxicity, high specific capacity (894 mAh g⁻¹), and its

commercial relevance as a primary battery cathode.^{23,24} While the majority of the work on FeS₂ revolves around liquid electrolyte systems, the use of a solid electrolyte has the added benefit of circumventing the issues of polysulfide shuttling and increased pressures improving particle contact.^{17,25} In addition, one advantage of the Fe-S system is the tendency for the Fe²⁺ to form nano-sized Fe⁰ clusters upon electrochemical reduction.²⁶ Electronically insulating Li₂S is also formed upon reduction and therefore the presence of an electronic framework provided by the Fe⁰ is critical to activate Li₂S redox.²⁷ Therefore, in exploring all solid-state batteries based on conversion metal sulfides, iron sulfides are a good starting point and there have already been a few reports of FeS₂^{17,25,28} and FeS²⁹ cells with sulfide solid electrolytes showing promising performance.

Inspired by the intermediate products (FeS and Li₂S) formed in FeS₂ cathodes, ^{30,31} in this work, the use of cation and anion conversion redox chemistry is explored as a means to maintain the high capacities enabled by multi-electron conversion reactions while benefiting from the improved electronic conductivities of the transition metal sulfide. While there have been recent reports of transition metal sulfides paired with Li₂S, the transition metal sulfide serves as an additive functioning as a redox mediator with only minor capacity contributions and primarily limited to intercalation sulfides (VS₂, MoS₂, WS₂, TiS₂).^{32,33} In contrast, this work explores the use of dual conversion system consisting of Li₂S and the transition metal sulfide FeS to benefit from multi-electron redox of both components, as well as an improved electronic conductivity from FeS, enabling the possibility to eliminate the need for carbon additives. Therefore, the ball milled (BM) FeS-Li₂S composites presented here demonstrates a different route to take on the challenges of poor electronic conductivity issues faced in Li-S SSB in addition to accessing multi-electron redox that provide much higher capacities relative to LiNi_{0.8}Co_{0.1}Mn_{0.1}O₂ or LiFePO₄ cathodes.

Experimental Section

Chemicals

FeS (Alfa Aesar, 99.9%), Li₂S (Alfa Aesar, 99.99%), Li₆PS₅CI (provided by AMG Lithium) powders and Li rods (abcr, 99.8 %) were transferred directly into an argon glove box (MBraun) under inert conditions (< 0.5 H₂O ppm, < 0.1 O₂ ppm). Vapor grown carbon nanofibers (Sigma-Aldrich) were first dried at 200 °C under vacuum for 24 hours before being transferred into the glovebox. Indium foil (chemPUR, 100 μ m thickness, 99.99%) was stored in a vacuum oven at 40 °C for at least two weeks prior to transfer into the glovebox.

Synthesis of 1:1 mol FeS:Li₂S active material composites

2.6 g total of total powder was ball milled (Fritsch Pulverisette 7 premium line) at 500 rpm (15 min on, 5 min off, direction reversal upon each cycle) in a 80 mL ZrO₂ milling cup with a ZrO₂ grinding media (Ø:3 mm) to powder ratio of 30:1.

Characterization of ball milled FeS:Li₂S composites

X-ray diffraction (XRD): Active material (FeS:Li₂S) and precursor powders (FeS, Li₂S) were sealed in capillaries (\varnothing : 0.5 mm) and measured using a StadiP X-Ray diffractometer from STOE in Debye-Scherrer geometry with a Mo-K α_1 radiation (λ = 0.7093 Å, , Ge(111) monochromator). Pair distribution function (PDF): Ball milled and shaker milled FeS:Li₂S active materials were measured in a sealed glass capillary with a STOE StadiP X-Ray diffractometer (Ag K α_1 radiation: λ = 0.5594 Å, Ge(111) monochromator) in Debye-Scherrer geometry with MYTHEN4K detectors. The scattering data were recorded over a Q-range of ~0.784 - 20.206 Å⁻¹ in steps of ~0.00294 Å⁻¹ for 24 h. An empty capillary was measured as the background with the same procedure. Then the X-ray diffraction data were background subtracted and converted to a pair distribution function with a Q-range cutoff of Q_{max} = 15 Å⁻¹ using PDFgetX3.

Scanning Electron Microscopy (SEM) and Energy Dispersive Spectroscopy (EDX): For the SEM investigations, an Auriga Crossbeam workstation (Carl-Zeiss) with a field emission gun (Schottkytype) was used with an acceleration voltage of 3 kV. The imaging process was conducted with an InLens secondary electron detector. In preparing the samples, the powdered forms were

dispersed, and the pressed pellets were mounted on carbon tape on SEM stubs. A thin layer of gold, approximately 10 nm thick, was sputtered onto the samples in an argon-filled glovebox to enhance the electronic conductivity. The samples were then transferred to the SEM vacuum chamber from the glovebox, using a specially designed SEM vacuum sample holder to minimize air exposure. For elemental composition analysis, EDX was carried out using an X-Max 80 mm² detector, with the system set to an acceleration voltage of 15 kV. The collected data was analyzed using INCA software (version 5.05, by Oxford Instruments).

Laser flash analysis (LFA): Pellets were prepared by isostatically pressing the powders (~150-200 mg) at 500 MPa for 60 min. The pellets were then carbon coated to ensure good emission and absorption properties and to protect the samples during transfer into the measurement chamber. Thermal diffusivities were then investigated using a LFA 467 *HyperFlash* (Netzsch-Gerätebau GmbH) with a MCT detector and a ZnS sample chamber window. A constant nitrogen flow (100 mL min⁻¹) was applied and a temperature range from -100 °C to 100 °C (stepsize ΔT = 25 °C) was investigated, whereby three measurements were conducted at each temperature step. All measurement signals were fitted with an improved Cape-Lehmann model to determine the temperature diffusivities using the NETZSCH software LFA Analysis 8.0.3. Further details and assumptions on thermal conductivity calculations can be found the Supporting Information.

Preparation of cathode composites

For cathode composites containing carbon additives were prepared by combining the active material (FeS:Li₂S, 1:1 mol) with vapor grown carbon nanofibers (CNF) and Li₆PS₅CI (LPSCI) solid electrolyte with a weight ratio of 30:20:50 a total powder mass of 200 mg. For the carbon-free composites, the active material and solid electrolyte were combined using a weight ratio of 50:50 with a total powder mass of 200 mg. For both compositions, the powders were placed in a

15 mL ZrO₂ cup with twenty ZrO₂ balls (∅: 3 mm) and shaker milled (Fritsch Pulverisette 23 Mini Mill) at a frequency of 45 Hz for 15 minutes.

Electrochemical cell assembly

All electrochemical measurements were performed using PEEK lined press cells with stainless steel stamps (\varnothing : 10 mm) as current collectors. For half-cell testing, the separator layer was formed by adding ~70 mg of solid electrolyte into the PEEK lining in between two stainless steel stamps and hand pressed. Subsequently, the cathode composite powder (10 - 20 mg) was evenly distributed on one side of the separator and uniaxially pressed at 370 MPa for 3 minutes. After densification, Li (~1.2 - 1.4 mg) and In foil (\varnothing : 9 mm) were added onto the other side of the separator with the indium foil in contact with the solid electrolyte. The cell was hand tightened and placed in a metal frame with an applied pressure of ~50 MPa (torque of 10 Nm) and left for 5 hours of at 25 °C prior to testing. For symmetric cell testing, the separator layer was formed as mentioned above and 10 mg of composite powder was added to each side prior to placing in the uniaxial press at 3 tons for 3 minutes and placed in the metal frame in the same manner as the half cells.

Electrochemical Characterization

All electrochemical characterization was performed on either a Biologic-VMP300 or Maccor 4000 with cells sitting inside a climate chamber maintained at 25°C. Half cells were cycled in a voltage window of 0.4 to 2.4 V (vs In/LiIn). All the C-rates in this study were determined using a theoretical capacity of 726 mAh g⁻¹ which takes into the mass of the Li in the complete four electron redox reaction. The exact current densities of each C-rate depend on the total capacity of the working electrode which depends on the weight fraction of active material in the composite and the total composite mass loading. For cyclic voltammetry experiments, half cells were assembled and cycled using a scan rate of 0.01 mV s⁻¹. To isolate Fe and S redox, the cell was cycled within the window of 1.4 to 0.4 V (vs In/LiIn) for Fe and 1.4 to 2.4 V (vs In/LiIn) vs for the S redox cell. For

symmetric cell testing, a voltage window of 0 V to 1.8 V and a current density of 0.14 mA cm $^{-2}$ was used. Assuming equal capacity contributions from Fe and S redox reactions, a voltage window of 1.8 V (\pm 0.9 V) in the symmetric cell would drive one electrode to delithiate up to \sim 2.3 V vs In/LiIn to undergo S redox while the other lithiates down to \sim 0.5 V vs In/LiIn to undergo Fe redox. Therefore, only one of the redox reactions are activated in each electrode and no more than half of the capacity can be obtained in the symmetric cell.

Effective partial conductivity measurements

DC (direct-current) polarization experiments were conducted to measure the effective electronic and ionic conductivities of the cathode composites. For electronic conductivity measurements, ~20 – 30 mg of composite powders were placed in a press cell in between two stainless steel stamps and pressed under a uniaxial pressure of 370 MPa for 3 minutes to densify the pellet. The cell was subsequently placed in a metal frame with an applied pressure of 50 MPa. The cell was left to rest for 5 hours prior to applying a series of potentials (+1 mV, -5 mV, +10 mV, -20 mV) for 3 hours each. For ionic conductivity measurements, the composite powder was sandwiched between two layers of solid electrolyte (80 mg) and pressed under a uniaxial pressure of 3 tons for 3 minutes. After densification, the cells were reopened and Li (~1.2 mg- 1.4 mg) and In foil (Ø: 9 mm) were added onto each end of the cell with the indium foil in contact with the solid electrolyte. The cell was subsequently placed in a metal frame with an applied pressure of 50 MPa and left to rest for 5 hours prior to applying a series of potentials (1 mV, 5 mV, 10 mV, 15 mV) for 8 hours each. The resulting current responses for both ion and electron blocking DC polarization measurements can be found in the Supporting Information.

Results & Discussion

FeS:Li₂S active material composites were synthesized via ball milling powders consisting of a 1:1 molar amounts of FeS and Li₂S (**Figure S1-S3**), similar to what is formed

electrochemically in FeS₂ during the irreversible initial lithiation reaction at elevated temperatures.^{24,34} The use of ball milling serves two main purposes: 1) for electrochemical activation of Li₂S and 2) ensure homogeneous mixing of the two components to form a composite. In regard to the first point, due to the low electrical (~ 10⁻⁹ S cm⁻¹) and ionic conductivity (~ 10⁻¹³ S cm⁻¹) of Li₂S, bulk Li₂S is generally electrochemically inactive and typically requires particles in the nanometer regime to activate redox.²⁷ Upon ball milling, particle size reduction is observed in the SEM, while EDX spectral mapping indicates a homogenous distribution (**Figure 1a, S5**). The concurrent reduction of Li₂S crystallite size is shown by the broadening of the Li₂S X-ray diffraction peaks in the composite (**Figure 1b, S2-S4**). The overlapping reflections prevent a Williamson-Hall analysis for the resulting particle size reduction and strain; therefore, pair distribution function analyses were performed. By comparing the crystalline starting materials Li₂S and FeS to the milled product, a reduction of the coherence length, which is strongly correlated to the damping profile of pair distribution function, is observed, further supporting the decrease in particle size (**Figure 1c**).

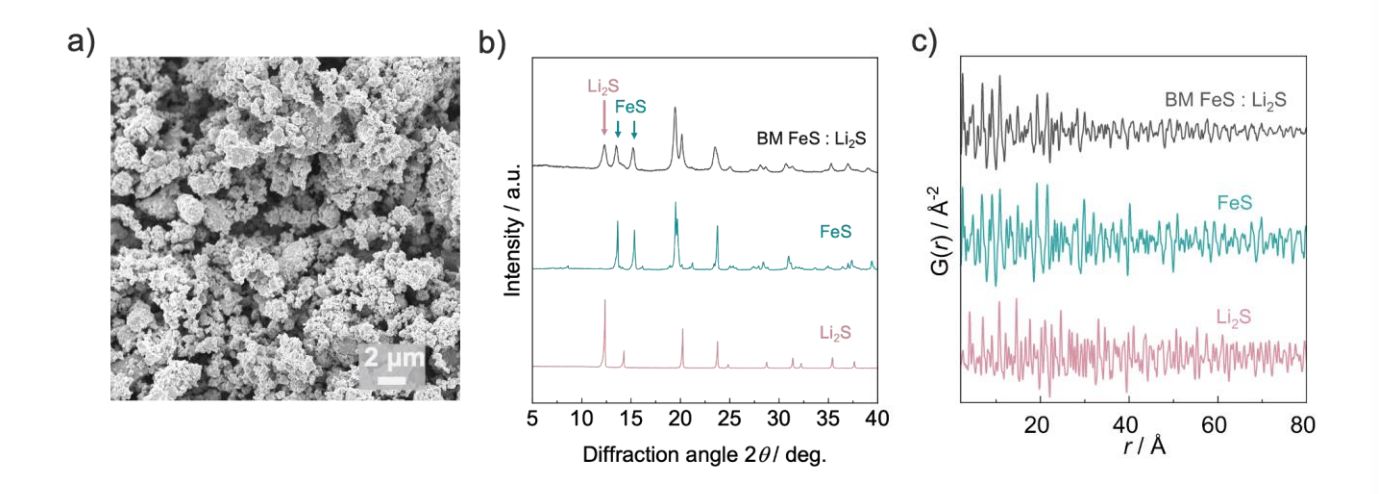


Figure 1. Characterization of BM FeS:Li₂S composites. (a) SEM of BM FeS:Li₂S powder (b) X-ray diffraction of BM FeS:Li₂S and precursor powders. (c) Pair distribution function of BM FeS:Li₂S powders which demonstrate decreased coherence length relative to precursor powders.

Initial electrochemical assessment of the ball milled FeS:Li₂S cathode composites was carried out using conductive carbon additives to first investigate the redox signatures of the active material while minimizing the influence of electronic conductivity which is typically poor in Li₂S-based cathodes. Ball milled active material powders were mixed together with vapor grown carbon nano fibers (CNF) and Li₆PS₅CI (LPSCI) in a shaker mill to mix all the components prior to being pelletized. SEM and EDX of the shaker milled composite powder and pressed pellet can be found in **Figure S6-S7**. CNF was chosen as the additive due to its good compatibility with sulfide solid electrolytes and minimal electrolyte decomposition in LPSCI-based all solid state batteries. ^{35,36} Given the two redox active components present in this system, FeS and Li₂S, there are two separate redox reactions at play: 1) FeS can undergo two electron cation redox from the reduction of Fe²⁺ to form Fe⁰ and additional Li₂S (Equation 1) and 2) the Li₂S initially present in the composite can undergo anion redox and undergo oxidation to form S₈ (Equation 2)³⁷:

Iron redox:
$$1 \text{ FeS} + 2 \text{ Li}^+ + 2 \text{ e}^- \rightleftharpoons 1 \text{ Fe}^0 + 1 \text{ Li}_2 \text{S}$$
 (Equation 1)

Sulfur redox:
$$1 \operatorname{Li}_2 S \rightleftharpoons \frac{1}{8} S_8 + 2 \operatorname{Li}^+ + 2 e^-$$
 (Equation 2)

Therefore, in its assembled state, the FeS:Li₂S half cells are in a partially lithiated state with an open circuit potential ~1.3 V vs In/Li-In. They can either be lithiated or delithiated in the first cycle in a two-electron redox process to either fully lithiate (Fe redox) or delithiate (S redox) the system (**Figure 2 a-b**). Subsequently, the cell undergoes a four-electron redox process from both the iron and sulfur redox. For example, in **Figure 2a**, during the first lithiation to 0.4 V vs In/Li-In, FeS is redox active and undergoes conversion to form Fe⁰ and additional Li₂S (Equ.1)³⁸ while the Li₂S originally present in FeS:Li₂S remains redox inactive in this initial potential window (~1.3 – 0.4 V vs In/Li-In). However, upon complete delithiation up to 2.4 V vs In/Li-In, both iron and sulfur redox

will be activated. The dual redox of FeS:Li₂S is further highlighted in Figure 2c showing two separate FeS:Li₂S half cells whereby one cell is lithiated first with a voltage window restricted to allow for only Fe redox while the other cell is delithiated first with a voltage window restricted to only allow for S redox. Due to the ability to separate the two redox processes by controlling the voltage window, a symmetric cell (FeS:Li₂S|LPSCI|FeS:Li₂S) can be demonstrated in which FeS:Li₂S served as both the anode and cathode, whereby the anode was limited to Fe redox and the cathode to S redox. The proof-of concept symmetric cell demonstrates >200 mAh g⁻¹ specific capacity with a working voltage window of 1.8 V (Figure 2d). If further optimized, in theory, the symmetric cell should be able to deliver half of the capacity of the four-electron process. The limited potential window half half-cell studies in Figure 2c indicate that the sulfur redox exhibits more capacity loss relative to the iron redox reactions. Therefore, the capacity fade observed in the symmetric cell (Figure 2d) more likely stems from the sulfur redox of the cathode over the iron redox in the anode. In addition, the sulfur cyclic voltammogram exhibits multiple peaks in the reduction process. The presence of multiple peaks could either be an indicator of intermediate species such as Li₂S₂ which has been recently detected to form alongside Li₂S in all solid-state batteries^{7,37} or partial LPSCI decomposition which shows some degree of reversibility.³⁶

FeS and Li₂S are reported to be intermediate products formed during the irreversible initial lithiation of FeS₂ system.^{38,39} Therefore, while FeS:Li₂S is chemically different from FeS₂, the electrochemical end products formed upon complete lithiation and delithiation should be the same as FeS₂ and can furthermore be viewed as an electrochemically-equivalent system to FeS₂.³⁴ Upon a complete lithiation, the reaction products should resemble Fe⁰ and Li₂S as reported extensively for the FeS₂ system while the delithiated products should contain a mixture of an iron sulfide and elemental sulfur.^{17,34,38,40} For solid-state FeS₂ cells, very few reports on phase identification of charge products exist, however, the formation of o-FeS₂, FeS_y, S₈ are among the most commonly referenced.¹⁷ While charge product identification is outside the scope of this work, the iron-sulfide charge product detected in the FeS:Li₂S system potentially resembles a

nanocrystalline Fe_3S_4 alongside another unidentifiable phase based on X-ray diffraction data (**Figure S8**). These charge products are similar to the ones detected in FeS_2 in ionic liquid electrolytes cells.³⁴

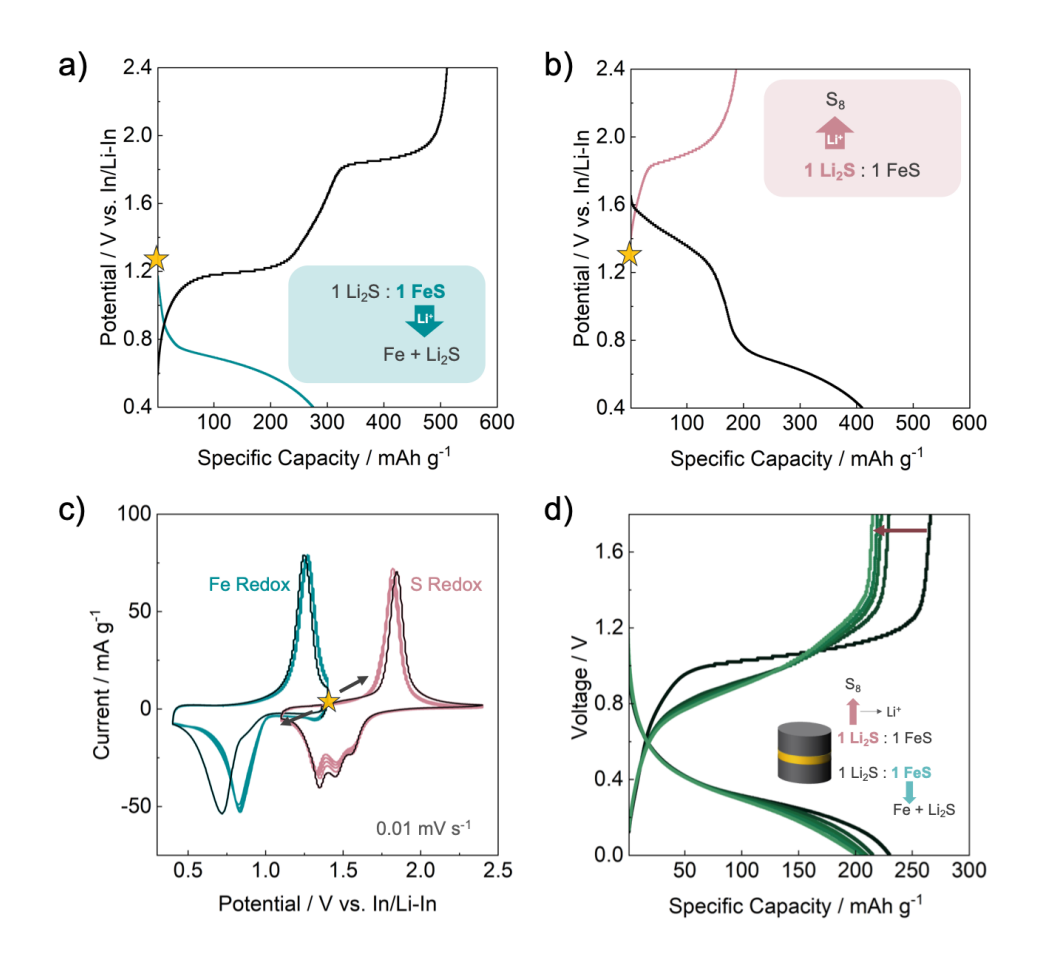


Figure 2. Electrochemical properties of FeS:Li₂S composites. In its assembled state, FeS:Li₂S composites can be either (a) lithiated first to reduce the FeS to form Fe⁰ or (b) delithiated first to oxidize Li₂S to form S₈. After the first lithiation or delithiation, the cell can undergo a four-electron redox process. The yellow star indicates the OCV. (c) Cyclic voltammograms of two separate FeS:Li₂S cells. The teal curve shows a cell with a potential window limited to only Fe redox while the pink curve shows S redox only. Black traces outline the first cycle. (d) Symmetric FeS:Li₂S solid-state cells cycled at C/10 assuming a two-electron redox reaction.

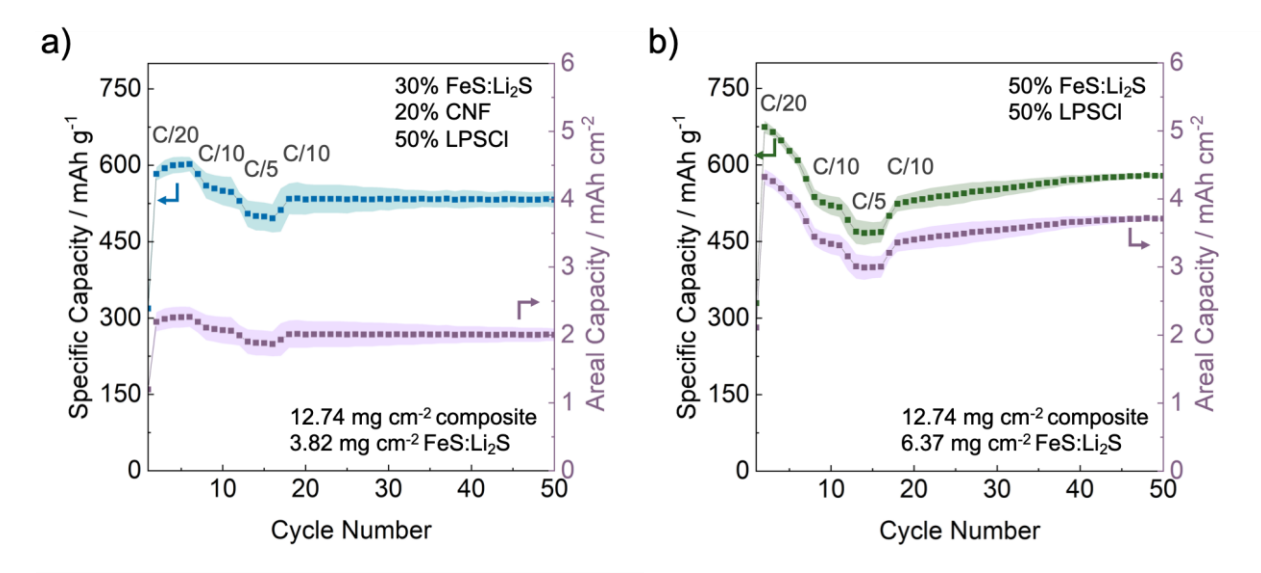


Figure 3. a) Electrochemical properties and performance of FeS:Li₂S SSB. C-rate performance of triplicate cells with a cathode composite loading of ~12.7 mg cm⁻² are shown for (a) FeS:Li₂S cells with CNF and (b) carbon-free FeS:Li₂S cells. For CNF containing cells, the areal current densities for C/20, C/10, C/5 are approximately 0.139, 0.277, 0.555 mA cm⁻², respectively. For carbon-free cells, the areal current densities for C/20, C/10, and C/5 are approximately 0.231, 0.462, and 0.924 mA cm⁻², respectively.

To assess the electrochemical performance of FeS:Li₂S SSB, triplicate half cells were assembled and tested, and individual cell data can be found in **Figure S9-S10**. C-rate testing of CNF-containing cathode composites demonstrates that at lower current densities of 0.139 mA cm⁻² (C/20), specific capacities of around 600 mAh g⁻¹ can be achieved while at higher current densities of 0.555 mA cm⁻² (C/5), capacities above 400 mAh g⁻¹ can be maintained across 50 cycles (**Figure S10**). The capacities achieved with CNF-containing FeS:Li₂S composites lie within the range of what is reported for all solid-state FeS and FeS₂ batteries (**Table S1**). While carbon additives and lower mass loadings help to establish FeS:Li₂S as a promising dual redox system, the ability to increase the active mass loading through the removal of carbon additives and increasing the cathode composite loading are important when considering the practical and commercial relevance of a system. In other words, while high specific capacities are critical, such benefits can be lost if the loadings cannot be increased to obtain high areal capacities. Therefore,

it is important to assess what areal capacities can be achieved with a given material system and in particular, carbon-free systems should help aid in higher active material loading per mass of composite powder. To this end, carbon-free FeS:Li₂S composites were also explored. SEM and EDX of the shaker milled composite powder and pressed pellet consisting of 50 wt% FeS:Li₂S and 50 wt% LPSCI can be found in **Figure S11-12**. **Figure 3b** shows the electrochemical performance of carbon-free FeS:Li₂S cells consisting of 50 wt% FeS:Li₂S and 50 wt% Li₆PS₅CI. Using the same total cathode composite loading of ~12.7 mg cm⁻² as with the carbon-containing composites, an active material loading of ~6.4 mg cm⁻² could be achieved with the carbon-free system. The achievable areal capacity at C/20 is ~2x greater than the carbon-containing cell for the same total composite cathode loading (12.7 mg_{composite} cm⁻²) but different active material loading (carbon-containing: 3.8 mg_{FeS:Li2S} cm⁻²; carbon-free: 6.4 mg_{FeS:Li2S} cm⁻²).

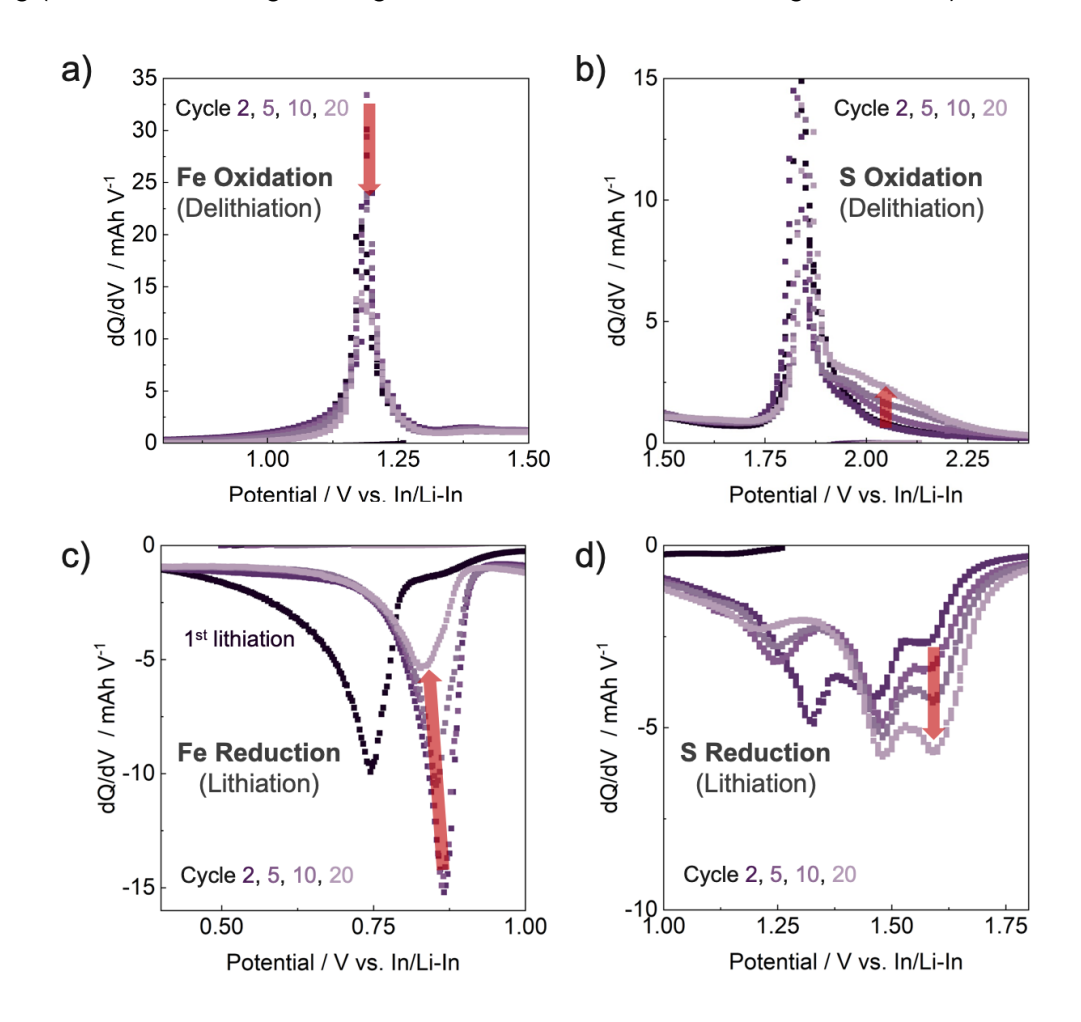


Figure 4. Capacity loss and degradation of carbon-free FeS:Li₂S SSB cycled at C/20 (0.139 mA cm⁻²). Zoom up dQ dV⁻¹ plots of the (a)-(b) delithiation and (c)-(d) lithiation cycles. The full dQ dV^{-1} can be found in **Figure S15**.

While the removal of carbon increases the areal capacity, capacity loss within the first few cycles were observed at lower currents (C/20) (Figure 3). In contrast, for C/5 cycling, initial cycle losses were minimal which suggests that degradation is more pronounced at slower currents (Figure S14). In order to understand the origins of capacity loss at lower C-rates, dQ dV⁻¹ analysis of a cell cycled at C/20 was employed to look at potentials where capacity changes could be detected. From the dQ dV⁻¹ analysis, the capacity loss can be identified from the iron redox upon lithiation as indicated by the reduced peak area at ~0.87 V vs. In/Li-In upon cycling (**Figure 4c**). In addition, peaks attributed to Li₂S redox are shown in Figure 4 b, d. Upon cycling, a broad shoulder ~ 2 V is seen to grow (Figure 4b) in addition to peak at ~1.6 V upon reduction (Figure 4d) which is attributed to sulfide solid electrolyte (Li₆PS₅Cl) decomposition rather than to the Li₂S redox. This can be corroborated by the change in relative capacities contributions from the iron and sulfur redox upon galvanostatic cycling. While FeS:Li₂S (1:1 mol) should have equal capacity stemming from the 2-electron redox of each component ($S^{2-} \leftrightarrow S^0$ and $Fe^{2+} \leftrightarrow Fe^0$), upon cycling, a shrinking Fe redox and growing S redox plateau is observed (Figure S13). Considering that equal capacity contributions are observed at the start of cycling, the continuous increase of capacity from the sulfur redox plateau must then originate from Li₆PS₅Cl decomposition. In addition, from dQ dV⁻¹ analysis, the oxidative Li₂S redox peak (**Figure 4b**) undergoes a shift to higher potentials indicating that upon cycling, the cell becomes more polarized and requires higher overpotentials for Li₂S redox. As for the Fe redox (Figure 4a), only a slight shift in peak potential is observed indicating less influence and change in overpotential is observed.

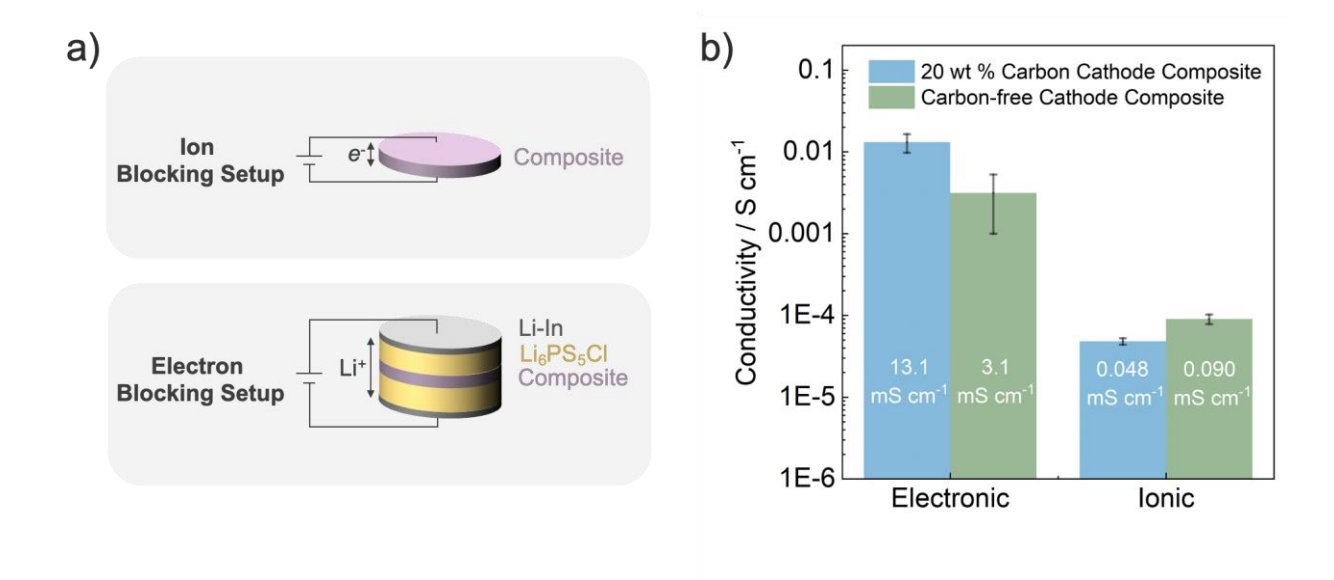


Figure 5. a) Schematic of sample configuration for DC polarization measurements to determine effective electronic (top) and ionic (bottom) conductivities of the cathode composites. (b) Ionic partial transport for CNF-containing (blue) and carbon-free (green) FeS:Li₂S cathode composites Comparison of partial electronic and ionic transport in CNF-containing and carbon-free FeS:Li₂S cathode composites. Error bars are from triplicate cells. I-V curves for all triplicate cells are shown in Figure S16-S17.

In regard to the higher achievable capacities in the carbon-free FeS:Li₂S, although the total composite loading is the same for both carbon and carbon-free systems, the active mass loading and thus capacity and C-rates used are different. Therefore, the current densities used in the carbon-free composites for a specific C-rate is ~1.67 times higher than the CNF-containing cell. Furthermore, the cathode composite morphologies are different, and the carbon-free composites contain higher density of smaller pores (Figure S6 and S11). Upon the volume expansion and contraction upon cycling, pulverization and contact loss could be further exacerbated by the presence of pore space. While the carbon-free system appears to undergo more solid electrolyte decomposition, the ability to achieve a much higher initial capacity at higher current densities is supported by the differences in partial transport between the CNF-containing and carbon-free FeS:Li₂S cathode composites. Figure 5 shows a side-by-side comparison of the

effective electronic and ionic conductivities between the two different cathode composites taken from triplicate cell measurements (Figure S16-S17). While CNF-containing FeS:Li₂S composites exhibit higher electronic conductivity relative to the carbon-free FeS:Li₂S composites, the ionic conductivity of both composite systems are several orders of magnitude lower. Therefore, it is the ionic conductivity that remains the bottleneck and improving upon the effective ion transport in the cathode composite can have a much larger influence on performance as shown by the higher capacities attainable in the carbon-free FeS:Li₂S despite the use of higher current densities.

To assess the limits for the active mass and composite loading in the carbon-free FeS:Li₂S system, an even higher cathode composite loading of 25.5 mg_{composite} cm⁻² (20.0 mg_{composite}) corresponding to an active mass loading of 12.7 mg_{FeS:Li2S} cm⁻² (10 mg_{FeS:Li2S}) was assembled into a cell. For these cells, capacity fading within the first few cycles were even greater than what was observed in the 6.4 mg cm⁻² active mass loading cells (**Figure S18**). Therefore, the comparison focuses on the 2nd cycle capacity obtained at C/20 across all various active mass loadings for triplicate cells which show that for higher mass loadings of 12.7 mg_{FeS:Li2S} cm⁻² areal capacities close to 7 mAh cm⁻² are achievable (**Figure S19**). Beyond increasing the total composite loading, an alternative to further increasing the areal capacity is to also look increasing the active material content in the cathode composite. While the carbon-free FeS:Li₂S were composed of 50 wt% FeS:Li₂S, it is possible to cycle cathode composites containing 70% FeS:Li₂S 30% LPSCI using slower current densities (**Figure S20**). Therefore, by tuning the active material ratios in the composite or scaling up the composite loading are two avenues in which areal capacities can be increased.

Thermal Properties of FeS: Li₂S

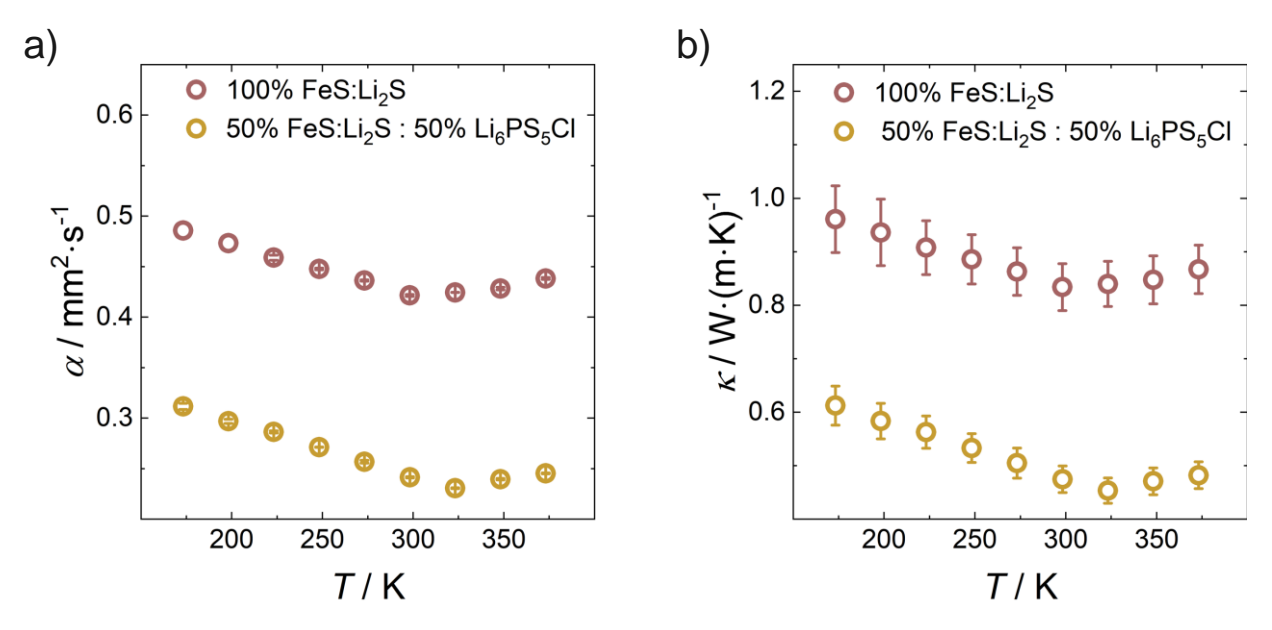


Figure 6. Thermal properties of BM FeS:Li₂S active material and cathode composites. a) Thermal diffusivity and (b) thermal conductivity of the FeS:Li₂S (red) and 50 wt% FeS:Li₂S 50 wt% Li₆PS₅Cl composite (yellow).

Lastly, in the transition to all solid-state batteries, open questions in regard to the thermal safety of solid-state battery systems at the active material, composite, cell, and pack level remain. 14 Under cell operation, the transport of charge carriers and electrochemical conversion reactions taking place generate heat. Since heat can highly influence battery performance and safety, understanding the transport and dissipation of heat away from heat sources are critical parameters for thermal management of batteries. 41 In a solid-state battery, the co-existence of various components (anode, cathode, solid electrolyte, carbon, pores, and current collectors) with varying thermal properties adds to the complexity of trying to understand the temperature distribution and heat pathways present under cell operation in addition to determining the best routes to improve upon heat dissipation. Focusing on the active material level, the majority of studies looking into thermal properties are dominated by intercalation chemistries due to their commercial relevance, while conversion chemistries receive very little attention. 42-44 In moving towards conversion chemistries and all solid-state systems, it is critical to assess the thermal

properties of such systems. To this end, thermal transport properties of active material (FeS:Li₂S) and cathode composite (50 wt% FeS:Li₂S & 50 wt% Li₆PS₅CI) pellets were investigated using laser flash analysis to obtain thermal diffusivities, which provides a measure of how quickly a material can spread temperature and is given by:

$$\alpha = \frac{\kappa}{\rho C_v}$$
 (Equation 3)

where α is thermal diffusivity, κ is thermal conductivity, ρ is the material density, and C_n is the specific isobaric heat capacity. Figure 6a shows the thermal diffusivity of the active material and cathode composite. The ball milled FeS:Li₂S active material demonstrates a higher thermal diffusivity relative to the cathode composite across the entire measured temperature range (-100 °C to 100 °C). The lower thermal diffusivity exhibited in the cathode composite is supported by the lower thermal diffusivity of the Li₆PS₅Cl, relative to FeS:Li₂S.⁴⁵ Based on those thermal diffusivities, thermal conductivities (Equation 3) of the active material and cathode composite were calculated based on the specific heat capacities estimated using the Dulong-Petit limit (Figure 6b, see Supporting Information). The thermal conductivity of the active material (FeS:Li₂S) is within the range of thermal conductivities reported for calendared carbon coated NCM622 and NCM811 sheets (~0.5 - 1 W m⁻¹ K⁻¹ at 20 °C)⁴⁶ and NCM532 electrodes (~0.5 W m⁻¹ K⁻¹).⁴⁷ It also is expected that the thermal conductivity of an NCM composite should also decrease with the introduction of Li₆PS₅Cl which is reported to exhibit lower thermal conductivities (~0.3 – 0.5 W m⁻¹ K⁻¹ at 20 °C).⁴⁵ While the thermal conductivity of the active material-electrolyte composite is low, the thermal conductivity of Li₆PS₅Cl is still within the same range as carbonate liquid electrolytes (~0.4-0.6 W m⁻¹ K⁻¹).47-49 Furthermore, even if NCM and FeS:Li₂S cathode composites have similar thermal conductivities, there is an inherent advantage from a thermal safety standpoint in that no gaseous decomposition products are expected to form in FeS:Li₂S unlike the case with NCM.^{2,3} While these initial results provide some insight on the material and composite level thermal properties that can help aid efforts in thermal modeling and management,

further work looking into how the thermal properties change upon various states of charge is needed. This is of particular importance for conversion electrodes in which the active material undergoes microstructural and phase changes which also have additional contributions to heat transport.⁵⁰

Conclusion

Conversion cathodes are promising class of cathode materials for next generation all solid-state batteries. The work presented offers an alternative route to achieve high areal capacities enabled by a dual cation and anion redox system, FeS:Li₂S, in order to address the issues of low electronic conductivity of pure sulfur cathodes while preserving the high capacities provided by multi-electron conversion redox reactions from both Fe and S redox. The electronic, ionic, and thermal transport of FeS:Li₂S composites are investigated. Further the electrochemical performance of FeS:Li₂S cells is evaluated and a carbon-free cathode composite achieving ~4 mAh cm⁻² is demonstrated. Lastly, a blueprint to further increase the areal capacities as high as ~7 mAh cm⁻² if further optimized (i.e. active material composition, total composite loading) are presented.

Supporting Information

X-ray diffraction data, scanning electron microscopy images, triplicate cell cycling data, thermal conductivity calculation details.

Acknowledgements

GW acknowledges funding from the Alexander von Humboldt foundation. The authors would like to also acknowledge AMG Lithium for providing the solid electrolyte and the support of BMBF MaSSiF under project number 03XP0519C. TZ and LK acknowledge funding from the Ministry of Culture and Science of the State North Rhine Westphalia in course of the International Graduate School of Battery Chemistry, Characterization, Analysis, Recycling and Application (BACCARA). The X-ray diffractometer was supported by the Deutsche Forschungsgemeinschaft (DFG) under project number 459785385.

References

- (1) IEA. Net Zero by 2050: A Roadmap for the Global Energy Sector. International Energy Agency. https://www.iea.org/reports/net-zero-by-2050 (accessed 2023-04-15).
- (2) Bartsch, T.; Strauss, F.; Hatsukade, T.; Schiele, A.; Kim, A. Y.; Hartmann, P.; Janek, J.; Brezesinski, T. Gas Evolution in All-Solid-State Battery Cells. ACS Energy Lett. 2018, 3 (10), 2539–2543. https://doi.org/10.1021/acsenergylett.8b01457.
- (3) Rui, X.; Ren, D.; Liu, X.; Wang, X.; Wang, K.; Lu, Y.; Li, L.; Wang, P.; Zhu, G.; Mao, Y.; Feng, X.; Lu, L.; Wang, H.; Ouyang, M. Distinct Thermal Runaway Mechanisms of Sulfide-Based All-Solid-State Batteries. *Energy Environ. Sci.* **2023**, *16* (8), 3552–3563. https://doi.org/10.1039/d3ee00084b.
- (4) Kim, T.; Kim, K.; Lee, S.; Song, G.; Jung, M. S.; Lee, K. T. Thermal Runaway Behavior of Li6PS5CI Solid Electrolytes for LiNi0.8Co0.1Mn0.1O2and LiFePO4in All-Solid-State Batteries. *Chem. Mater.* 2022, 34 (20), 9159–9171. https://doi.org/10.1021/acs.chemmater.2c02106.
- (5) Cronk, A.; Chen, Y. T.; Deysher, G.; Ham, S. Y.; Yang, H.; Ridley, P.; Sayahpour, B.; Nguyen, L. H. B.; Oh, J. A. S.; Jang, J.; Tan, D. H. S.; Meng, Y. S. Overcoming the Interfacial Challenges of LiFePO4 in Inorganic All-Solid-State Batteries. ACS Energy Lett. 2023, 8 (1), 827–835. https://doi.org/10.1021/acsenergylett.2c02138.
- (6) Sun, K.; Cao, C.; Zhao, D.; Tong, X.; Bak, S.; Du, Y.; Wang, F.; Steingart, D. A. Degradation of Lithium Iron Phosphate Sulfide Solid-State Batteries by Conductive Interfaces. J. Phys. Chem. C 2023, 127 (39), 19396–19405.
 https://doi.org/10.1021/acs.jpcc.3c05039.
- (7) Kim, J. T.; Rao, A.; Nie, H. Y.; Hu, Y.; Li, W.; Zhao, F.; Deng, S.; Hao, X.; Fu, J.; Luo, J.; Duan, H.; Wang, C.; Singh, C. V.; Sun, X. Manipulating Li2S2/Li2S Mixed Discharge Products of All-Solid-State Lithium Sulfur Batteries for Improved Cycle Life. *Nat. Commun.* 2023, 14 (1). https://doi.org/10.1038/s41467-023-42109-5.

- (8) Ohno, S.; Zeier, W. G. Toward Practical Solid-State Lithium-Sulfur Batteries: Challenges and Perspectives. *Accounts Mater. Res.* 2021, 2 (10), 869–880. https://doi.org/10.1021/accountsmr.1c00116.
- (9) Wang, D.; Jhang, L. J.; Kou, R.; Liao, M.; Zheng, S.; Jiang, H.; Shi, P.; Li, G. X.; Meng, K.; Wang, D. Realizing High-Capacity All-Solid-State Lithium-Sulfur Batteries Using a Low-Density Inorganic Solid-State Electrolyte. *Nat. Commun.* 2023, 14 (1), 1–10. https://doi.org/10.1038/s41467-023-37564-z.
- (10) Ohno, S.; Rosenbach, C.; Dewald, G. F.; Janek, J.; Zeier, W. G. Linking Solid Electrolyte Degradation to Charge Carrier Transport in the Thiophosphate-Based Composite Cathode toward Solid-State Lithium-Sulfur Batteries. *Adv. Funct. Mater.* 2021. https://doi.org/10.1002/adfm.202010620.
- (11) Gao, X.; Zheng, X.; Tsao, Y.; Zhang, P.; Xiao, X.; Ye, Y.; Li, J.; Yang, Y.; Xu, R.; Bao, Z.; Cui, Y. All-Solid-State Lithium-Sulfur Batteries Enhanced by Redox Mediators. *J. Am. Chem. Soc.* 2021, 143 (43), 18188–18195. https://doi.org/10.1021/jacs.1c07754.
- (12) Xu, S.; Kwok, C. Y.; Zhou, L.; Zhang, Z.; Kochetkov, I.; Nazar, L. F. A High Capacity All Solid-State Li-Sulfur Battery Enabled by Conversion-Intercalation Hybrid Cathode Architecture. Adv. Funct. Mater. 2021, 31 (2), 2004239.
 https://doi.org/10.1002/adfm.202004239.
- (13) Fujita, Y.; Hakari, T.; Sakuda, A.; Deguchi, M.; Kawasaki, Y.; Tsukasaki, H.; Mori, S.; Tatsumisago, M.; Hayashi, A. Li2S-Lil Solid Solutions with Ionic Conductive Domains for Enhanced All-Solid-State Li/S Batteries. ACS Appl. Energy Mater. 2022, 5 (8), 9429– 9436. https://doi.org/10.1021/acsaem.2c00978.
- (14) Whang, G.; Zeier, W. G. Transition Metal Sulfide Conversion: A Promising Approach to Solid-State Batteries. ACS Energy Lett. 2023, 8 (12), 5264–5274. https://doi.org/10.1021/acsenergylett.3c02246.
- (15) Zhang, Z.; Dong, K.; Mazzio, K. A.; Hilger, A.; Markötter, H.; Wilde, F.; Heinemann, T.;

- Manke, I.; Adelhelm, P. Phase Transformation and Microstructural Evolution of CuS Electrodes in Solid-State Batteries Probed by In Situ 3D X-Ray Tomography. *Adv. Energy Mater.* **2023**, *13* (2), 2203143. https://doi.org/10.1002/aenm.202203143.
- (16) Santhosha, A. L.; Nazer, N.; Koerver, R.; Randau, S.; Richter, F. H.; Weber, D. A.; Kulisch, J.; Adermann, T.; Janek, J.; Adelhelm, P. Macroscopic Displacement Reaction of Copper Sulfide in Lithium Solid-State Batteries. *Adv. Energy Mater.* 2020, 10 (41), 1–9. https://doi.org/10.1002/aenm.202002394.
- (17) Yersak, T. A.; Macpherson, H. A.; Kim, S. C.; Le, V. D.; Kang, C. S.; Son, S. B.; Kim, Y. H.; Trevey, J. E.; Oh, K. H.; Stol dt, C.; Lee, S. H. Solid State Enabled Reversible Four Electron Storage. *Adv. Energy Mater.* 2013, 3 (1), 120–127. https://doi.org/10.1002/aenm.201200267.
- (18) Takada, K. Solid State Batteries with Sulfide-Based Solid Electrolytes. *Solid State Ionics* **2004**, *172* (1–4), 25–30. https://doi.org/10.1016/j.ssi.2004.02.027.
- (19) Takada, K. Lithium Iron Sulfide as an Electrode Material in a Solid State Lithium Battery. Solid State Ionics 1999, 117 (3–4), 273–276. https://doi.org/10.1016/S0167-2738(98)00413-5.
- (20) Butala, M. M.; Mayo, M.; Doan-Nguyen, V. V. T.; Lumley, M. A.; Göbel, C.; Wiaderek, K. M.; Borkiewicz, O. J.; Chapman, K. W.; Chupas, P. J.; Balasubramanian, M.; Laurita, G.; Britto, S.; Morris, A. J.; Grey, C. P.; Seshadri, R. Local Structure Evolution and Modes of Charge Storage in Secondary Li-FeS2 Cells. *Chem. Mater.* 2017, 29 (7), 3070–3082. https://doi.org/10.1021/acs.chemmater.7b00070.
- (21) Yersak, T. A.; Macpherson, H. A.; Kim, S. C.; Le, V. D.; Kang, C. S.; Son, S. B.; Kim, Y. H.; Trevey, J. E.; Oh, K. H.; Stol dt, C.; Lee, S. H. Solid State Enabled Reversible Four Electron Storage. Adv. Energy Mater. 2013, 3 (1), 120–127. https://doi.org/10.1002/aenm.201200267.
- (22) Boebinger, M. G.; Yeh, D.; Xu, M.; Miles, B. C.; Wang, B.; Papakyriakou, M.; Lewis, J. A.;

- Kondekar, N. P.; Cortes, F. J. Q.; Hwang, S.; Sang, X.; Su, D.; Unocic, R. R.; Xia, S.; Zhu, T.; McDowell, M. T. Avoiding Fracture in a Conversion Battery Material through Reaction with Larger Ions. *Joule* **2018**, *2* (9), 1783–1799. https://doi.org/10.1016/j.joule.2018.05.015.
- (23) Rickard, D.; Luther, G. W. Chemistry of Iron Sulfides. *Chem. Rev.* 2007, 107 (2), 514–562. https://doi.org/10.1021/cr0503658.
- (24) Fong, R.; Dahn, J. R.; Jones, C. H. W. Electrochemistry of Pyrite-Based Cathodes for Ambient Temperature Lithium Batteries. *J. Electrochem. Soc.* **1989**, *136* (11), 3206–3210. https://doi.org/10.1149/1.2096426.
- (25) Dewald, G. F.; Liaqat, Z.; Lange, M. A.; Tremel, W.; Zeier, W. G. Influence of Iron Sulfide Nanoparticle Sizes in Solid-State Batteries**. *Angew. Chemie Int. Ed.* **2021**, *60* (33), 17952–17956. https://doi.org/10.1002/anie.202106018.
- (26) Butala, M. M.; Mayo, M.; Doan-Nguyen, V. V. T.; Lumley, M. A.; Göbel, C.; Wiaderek, K. M.; Borkiewicz, O. J.; Chapman, K. W.; Chupas, P. J.; Balasubramanian, M.; Laurita, G.; Britto, S.; Morris, A. J.; Grey, C. P.; Seshadri, R. Local Structure Evolution and Modes of Charge Storage in Secondary Li-FeS2 Cells. *Chem. Mater.* 2017, 29 (7), 3070–3082. https://doi.org/10.1021/acs.chemmater.7b00070.
- (27) Ye, H.; Li, M.; Liu, T.; Li, Y.; Lu, J. Activating Li2S as the Lithium-Containing Cathode in Lithium-Sulfur Batteries. *ACS Energy Lett.* **2020**, *5* (7), 2234–2245. https://doi.org/10.1021/acsenergylett.0c00936.
- (28) Shen, C.; Liu, Y.; Shi, Y.; Liu, X.; Jiang, Y.; Huang, S.; Zhang, J.; Zhao, B. Construction of Ion–Electron Conduction Network on FeS2 as High-Performance Cathodes Enables All-Solid-State Lithium Batteries. *J. Colloid Interface Sci.* **2024**, *653* (PA), 85–93. https://doi.org/10.1016/j.jcis.2023.09.048.
- (29) Kim, B. C.; Takada, K.; Ohta, N.; Seino, Y.; Zhang, L.; Wada, H.; Sasaki, T. All Solid State Li-Ion Secondary Battery with FeS Anode. *Solid State Ionics* **2005**, *176* (31–34),

- 2383–2387. https://doi.org/10.1016/j.ssi.2005.05.019.
- (30) Zou, J.; Zhao, J.; Wang, B.; Chen, S.; Chen, P.; Ran, Q.; Li, L.; Wang, X.; Yao, J.; Li, H.; Huang, J.; Niu, X.; Wang, L. Unraveling the Reaction Mechanism of FeS2as a Li-Ion Battery Cathode. ACS Appl. Mater. Interfaces 2020, 12 (40), 44850–44857. https://doi.org/10.1021/acsami.0c14082.
- (31) Whang, G.; Ashby, D. S.; Lapp, A. S.; Hsieh, Y.-C.; Butts, D. M.; Kolesnichenko, I. V; Wu, P.-W.; Lambert, T. N.; Talin, A. A.; Dunn, B. S. Temperature-Dependent Reaction Pathways in FeS 2: Reversibility and the Electrochemical Formation of Fe 3 S 4. *Chem. Mater.* 2022, 34 (12), 5422–5432. https://doi.org/10.1021/acs.chemmater.2c00291.
- (32) Gamo, H.; Hikima, K.; Matsuda, A. Transition-Metal Sulfides for High-Performance Lithium Sulfide Cathodes in All-Solid-State Lithium-Sulfur Batteries. ACS Omega 2023. https://doi.org/10.1021/acsomega.3c05635.
- (33) Kwok, C. Y.; Xu, S.; Kochetkov, I.; Zhou, L.; Nazar, L. F. High-Performance All-Solid-State Li2S Batteries Using an Interfacial Redox Mediator. *Energy Environ. Sci.* 2023, 16 (2), 610–618. https://doi.org/10.1039/d2ee03297j.
- (34) Whang, G.; Ashby, D. S.; Lapp, A. S.; Hsieh, Y.-C.; Butts, D. M.; Kolesnichenko, I. V.; Wu, P.-W.; Lambert, T. N.; Talin, A. A.; Dunn, B. S. Temperature-Dependent Reaction Pathways in FeS 2: Reversibility and the Electrochemical Formation of Fe 3 S 4. *Chem. Mater.* 2022, 34 (12), 5422–5432. https://doi.org/10.1021/acs.chemmater.2c00291.
- (35) Rana, M.; Rudel, Y.; Heuer, P.; Schlautmann, E.; Rosenbach, C.; Ali, M. Y.; Wiggers, H.; Bielefeld, A.; Zeier, W. G. Toward Achieving High Areal Capacity in Silicon-Based Solid-State Battery Anodes: What Influences the Rate-Performance? *ACS Energy Lett.* **2023**, *8* (7), 3196–3203. https://doi.org/10.1021/acsenergylett.3c00722.
- (36) Tan, D. H. S.; Wu, E. A.; Nguyen, H.; Chen, Z.; Marple, M. A. T.; Doux, J. M.; Wang, X.; Yang, H.; Banerjee, A.; Meng, Y. S. Elucidating Reversible Electrochemical Redox of Li6PS5CI Solid Electrolyte. ACS Energy Lett. 2019, 2418–2427.

- https://doi.org/10.1021/acsenergylett.9b01693.
- (37) Cao, D.; Sun, X.; Li, F.; Bak, S. M.; Ji, T.; Geiwitz, M.; Burch, K. S.; Du, Y.; Yang, G.; Zhu, H. Understanding Electrochemical Reaction Mechanisms of Sulfur in All-Solid-State Batteries through Operando and Theoretical Studies**. *Angew. Chemie Int. Ed.* 2023, 62 (20). https://doi.org/10.1002/anie.202302363.
- (38) Zou, J.; Zhao, J.; Wang, B.; Chen, S.; Chen, P.; Ran, Q.; Li, L.; Wang, X.; Yao, J.; Li, H.; Huang, J.; Niu, X.; Wang, L. Unraveling the Reaction Mechanism of FeS 2 as a Li-Ion Battery Cathode. ACS Appl. Mater. Interfaces 2020, 12 (40), 44850–44857. https://doi.org/10.1021/acsami.0c14082.
- (39) Tryk, D. A.; Kim, S.; Hu, Y.; Xing, W.; Scherson, D. A.; Antonio, M. R.; Leger, V. Z.; Blomgren, G. E. *Electrochemical Insertion of Lithium into Pyrite from Nonaqueous Electrolytes at Room Temperature: An in Situ Fe K-Edge X-Ray Absorption Fine Structure Study*; 1995; Vol. 99.
- (40) Zhang, S. S. The Redox Mechanism of FeS2 in Non-Aqueous Electrolytes for Lithium and Sodium Batteries. *Journal of Materials Chemistry A*. Royal Society of Chemistry April 21, 2015, pp 7689–7694. https://doi.org/10.1039/c5ta00623f.
- (41) Agne, M. T.; Böger, T.; Bernges, T.; Zeier, W. G. Importance of Thermal Transport for the Design of Solid-State Battery Materials. *PRX Energy* 2022, 10 (1), 1. https://doi.org/10.1103/PRXEnergy.1.031002.
- (42) Heubner, C.; Schneider, M.; Michaelis, A. Detailed Study of Heat Generation in Porous LiCoO2 Electrodes. J. Power Sources 2016, 307, 199–207. https://doi.org/10.1016/j.jpowsour.2015.12.096.
- (43) Zhang, X.; Sastry, A. M.; Shyy, W. Intercalation-Induced Stress and Heat Generation within Single Lithium-Ion Battery Cathode Particles. *J. Electrochem. Soc.* 2008, 155 (7), A542. https://doi.org/10.1149/1.2926617.
- (44) Lin, C.; Wang, F.; Fan, B.; Ren, S.; Zhang, Y.; Han, L.; Liu, S.; Xu, S. Comparative Study

- on the Heat Generation Behavior of Lithium-Ion Batteries with Different Cathode Materials Using Accelerating Rate Calorimetry. *Energy Procedia* **2017**, *142*, 3369–3374. https://doi.org/10.1016/j.egypro.2017.12.472.
- (45) Böger, T.; Bernges, T.; Li, Y.; Canepa, P.; Zeier, W. G. Thermal Conductivities of Lithiumlon-Conducting Solid Electrolytes. ACS Appl. Energy Mater. 2023, 6 (20), 10704–10712. https://doi.org/10.1021/acsaem.3c01977.
- (46) Gandert, J. C.; Müller, M.; Paarmann, S.; Queisser, O.; Wetzel, T. Effective Thermal Conductivity of Lithium-Ion Battery Electrodes in Dependence on the Degree of Calendering. *Energy Technol.* 2023, 11 (8), 1–12. https://doi.org/10.1002/ente.202300259.
- (47) Spitthoff, L.; Wahl, M. S.; Vie, P. J. S.; Burheim, O. S. Thermal Transport in Lithium-Ion Batteries: The Effect of Degradation. *J. Power Sources* 2023, 577 (February), 233149. https://doi.org/10.1016/j.jpowsour.2023.233149.
- (48) Guo, G.; Long, B.; Cheng, B.; Zhou, S.; Xu, P.; Cao, B. Three-Dimensional Thermal Finite Element Modeling of Lithium-Ion Battery in Thermal Abuse Application. *J. Power Sources* **2010**, *195* (8), 2393–2398. https://doi.org/10.1016/j.jpowsour.2009.10.090.
- (49) Burheim, O. S.; Onsrud, M. A.; Pharoah, J. G.; Vullum-Bruer, F.; Vie, P. J. S. Thermal Conductivity, Heat Sources and Temperature Profiles of Li-lon Secondary Batteries. ECS Meet. Abstr. 2013, MA2013-02 (14), 1190–1190. https://doi.org/10.1149/ma2013-02/14/1190.
- (50) Shin, J.; Kim, S.; Park, H.; Won Jang, H.; Cahill, D. G.; Braun, P. V. Thermal Conductivity of Intercalation, Conversion, and Alloying Lithium-Ion Battery Electrode Materials as Function of Their State of Charge. *Curr. Opin. Solid State Mater. Sci.* **2022**, *26* (2). https://doi.org/10.1016/j.cossms.2021.100980.

For table of contents only

